

PAPER • OPEN ACCESS

Disentangling the intrinsic relaxivities of highly purified graphene oxide

To cite this article: Giulia Fioravanti *et al* 2024 *Nanotechnology* **35** 245101

View the [article online](#) for updates and enhancements.

You may also like

- [Proton magnetization relaxation in aqueous suspensions of composite silicon-iron nanoparticles for biomedical applications](#)
Yu V Kargina, A D Mironova, A Yu Kharin et al.
- [Paramagnetic perfluorocarbon-filled albumin-\(Gd-DTPA\) microbubbles for the induction of focused-ultrasound-induced blood–brain barrier opening and concurrent MR and ultrasound imaging](#)
Ai-Ho Liao, Hao-Li Liu, Chia-Hao Su et al.
- [Effects of magnetic field strength and particle aggregation on relaxivity of ultra-small dual contrast iron oxide nanoparticles](#)
Hang T Ta, Zhen Li, Yuao Wu et al.



The Electrochemical Society

Advancing solid state & electrochemical science & technology

DISCOVER
how sustainability
intersects with
electrochemistry & solid
state science research



Disentangling the intrinsic relaxivities of highly purified graphene oxide

Giulia Fioravanti¹ , Angelo Galante^{2,3,4} , Paola Fattibene⁵ ,
Laura Torrieri Di Tullio^{5,6} , Silvia Colacicchi² , Giorgio De Thomasi² ,
Francesco Perrozzì¹, Niccolò De Berardinis², Gianni Profeta^{1,4} ,
Luca Ottaviano^{1,4}  and Marcello Alecci^{2,3,4} 

¹ Department of Physical and Chemical Sciences, University of L'Aquila, I-67100 L'Aquila, Italy

² Department of Life, Health and Environmental Sciences, University of L'Aquila, I-67100 L'Aquila, Italy

³ National Institute for Nuclear Physics (INFN), Gran Sasso National Laboratory (LNGS), I-67100 L'Aquila, Italy

⁴ CNR-SPIN, c/o Department of Physical and Chemical Sciences, I-67100 L'Aquila, Italy

⁵ Istituto Superiore di Sanità, Core Facilities, Viale Regina Elena 299, I-00161 Rome, Italy

⁶ Department of Biochemical Sciences 'A. Rossi Fanelli', Sapienza University of Rome, Viale Regina Elena 332, I-00185 Rome, Italy

E-mail: angelo.galante@univaq.it

Received 16 October 2023, revised 13 February 2024

Accepted for publication 10 March 2024

Published 3 April 2024



CrossMark

Abstract


The chemistry of contrast agents (CAs) for magnetic resonance imaging (MRI) applications is an active area of research and, in recent work, it was shown that CA-based graphene oxide (GO) has valuable properties for biomedical uses. GO has a potential as MRI CAs thanks to several functionalities, like its ability to penetrate tissues and cell membranes, as well as easy coupling with therapeutic agents, therefore showing the potential for both a diagnostic and therapeutic role. In this study, we performed a thorough cleaning of the GO sample (synthesized using a modified Hummers method), minimizing the amount of residual manganese down to 73 ppm. Using a wide range of physical–chemical methods (morphology, chemical composition, elemental analysis, spectroscopies, and imaging), we characterized the intrinsic longitudinal and transverse relaxivities of highly purified GO nanosheets. X-band electron paramagnetic resonance allowed to recognize the paramagnetic species involved, and 1.0 T MRI was used to disentangle the relative contributions to the MRI contrast of pristine GO nanosheets arising from structural defects and residual paramagnetic manganese impurities embedded in the nanomaterial. Although experiments show that the MRI relaxivity of GO nanosheets arises from the cumulative effect of structural defects and paramagnetic impurities, we conclude that the latter contribution to the longitudinal and transverse relaxivities becomes irrelevant for highly purified (pristine) GO. This novel finding clearly demonstrates that, apart from trivial manganese inclusion, pristine GO produces an inherent MRI response via structural defects, and therefore it is on its own a suitable candidate as MRI contrast agent.

Supplementary material for this article is available [online](#)

Keywords: contrast agents, graphene oxide, manganese, dangling bonds, MRI, EPR

Introduction

Since the discovery of graphene [1] and the development of its derivatives, graphene-based biocompatible materials have emerged as a powerful tool for a wide range of biomedical

 Original content from this work may be used under the terms of the [Creative Commons Attribution 4.0 licence](#). Any further distribution of this work must maintain attribution to the author(s) and the title of the work, journal citation and DOI.

applications, such as biosensing, imaging, nanocarriers, drug delivery, and cancer treatment, due to their unique 2D structure and versatile surface chemistry, that allows tunable physical/chemical properties [2, 3]. Graphene oxide (GO) shows relevant mechanical, thermal, electrical, optical, magnetic, biological properties, and compared to graphene, a higher degree of oxidation allowing versatile biomedical functionalization [4]. Several nanoparticles can be loaded/anchored onto the surface of graphene/GO to provide additional functional properties, useful, for example, for bioimaging and cancer therapy [5]. For instance, iron oxide nanoparticles showing excellent magnetic properties have been integrated with graphene for magnetic resonance imaging (MRI) and magnetic hyperthermia studies [6].

The wide range of endogenous MRI contrast mechanisms (proton density, longitudinal relaxation time T_1 , transverse relaxation time T_2 , diffusion, perfusion, etc.) have been expanded by means of exogenous CAs, i.e. material constructs containing paramagnetic atoms capable to modify, via intermolecular dipolar interactions, the intrinsic relaxation times of the tissues' water molecules [7]. Complexes of paramagnetic metal ions, such as gadolinium (Gd^{3+}), manganese (Mn^{2+}), iron (Fe^{2+}) are often used as CAs [8, 9]. To compare the effectiveness of CAs, the molar longitudinal (r_1) or transverse (r_2) relaxivities in water are defined as the $1/T_1$ (s^{-1}) or $1/T_2$ (s^{-1}) change rate per unit concentration (mM), respectively.

Contrast agents are broadly classified based on their effect in standard imaging sequences. Gd chelated paramagnetic CAs, widely used in the clinical practice, are the prototype of the first CA class. They have large relaxivities (typically $3 \div 30 \text{ mM} \cdot \text{s}^{-1}$ @ 1.5 T) with small $r_2/r_1 \sim 1 \div 2$ [10], are used in T_1 -weighted acquisitions to enhance tissue signal and classified as positive or T_1 agents. Superparamagnetic/magnetic nanoparticles based on iron oxides particles are the prototype of the second CA class. They have r_1 like the previous ones but larger r_2 with $r_2/r_1 \sim 4 \div 120$ [11], are used in T_2 -weighted acquisitions to suppress tissue signal and are classified as negative or T_2 agents. More recently bimodal T_1 – T_2 CAs using functionalized magnetic nanoparticles hosting complexes of both categories have been proposed to acquire more detailed information or disambiguate image artefacts [12].

The clinical use of Gd(III) chelate-based T_1 MRI CAs has steadily increased in the last 25 years, together with the diffusion of diseases requiring their use, including nephrogenic systemic fibrosis and higher renal retention with impaired kidney function [8]. At the same time, there is a strong need for T_1 MRI CAs that are safer and more effective, and novel CAs employing Mn(II) ions have been proposed as possible alternatives [9]. The non-lanthanide metal Mn is a natural cellular constituent, and often acts as a cofactor for enzymes and receptors. When used as CA, Mn(II) is capable of shortening the T_2 of water protons, while has a minor T_1 effect [13].

Notably, free Mn(II) ions are toxic at high concentrations (for example Mn detection of cortical layers in mouse brain was demonstrated at concentration above 88 ppm [9]) or after

long-term exposure, and can cause the neurodegenerative disorder known as 'manganism', with symptoms similar to Parkinson's disease [14]. However, their toxicity can be reduced by the formation of chelates with organic ligand such as dipyriddyoxyl diphosphate (DPDP) [15].

The development of metal ion-carbon nanostructure complexes has opened new opportunities for developing a novel class of MRI CAs with innovative functionalities [5, 16–19]. Magnetic GO nanosheets composite, decorated with magnetite [20] or gadolinium ions [21], have been used as CAs for *in vitro* and *in vivo* MRI cell tracking [22]. However, the full characterization and understanding of the T_1 and T_2 relaxation mechanisms of GO in water are still not thoroughly understood [23–25], and there are concerns about their long-term *in vivo* safety [26]. Previous works focused on the magnetic property alterations of pristine GO nanosheets due to the presence of metallic impurities [27, 28]. Their presence derives from both the initial graphite material and the synthesis processes. In fact, commonly GO nanosheets are obtained by oxidizing graphite to graphite oxide and exfoliating it. Several GO synthesis methods can be carried out, which are broadly classified as chlorate or permanganate-based [28]. In the latter method, metal-based molecules are required, with the drawback of adding significant quantities of metallic impurities. Wong *et al* [28] reported 2290 ppm of manganese, as well as many other metals at lower concentrations (identified by elemental analysis) in GO synthesized by the Hummers method (permanganate-based). Since these impurities present high affinity to the graphenic carbon atoms, it is very hard to totally remove them in the final product, leaving a large degree of uncertainty in the physical-chemical properties of GO nanosheets related to the level of remnant impurities.

A proper quantification and characterization of metallic impurities embedded in GO is of paramount importance to ensure that their presence does not hamper the specific use for which the nanosheets are intended. The presence of manganese impurities and their MRI relaxivity effects were studied by means of spectroscopic and EPR/MRI methods [16, 29–31]. However, the specific manganese impurity interactions with the GO nanosheets in water and their role as an effective mean to tune the T_1 and/or T_2 relaxation times of water is still an open question in the research field of GO-based CAs.

Through a careful analysis of the literature, we noticed that most of previous works involving the use of MRI CAs GO-based materials are based on GO/paramagnetic metal composites, using manganese, iron and gadolinium, or mixtures thereof [18, 20, 21, 32, 33], showed a wide range of measured relaxivities variability: r_1 ($9\text{--}92 \text{ mM}^{-1} \text{ s}^{-1}$) and r_2 ($97\text{--}171 \text{ mM}^{-1} \text{ s}^{-1}$) [16–18].

In this work we have focused our investigation to the MRI relaxation effects of both Mn(II) impurities, due to the production process, and to the paramagnetic dangling bonds present at the edge of nanoholes in pristine GO. Interestingly, to the best of our knowledge, there are only three reports, describing the MRI characterization of pristine GO, i.e. as synthesized with the modified Hummers method, and without ad hoc manganese enrichment [34–36].

The effects of localized spins of carbon-inherited defects (dangling bonds) on the magnetic properties of GO have been previously reported [29, 34]. Li *et al* [34] were able to experimentally adjust the number of nanoholes on GO nanosheets, showing that their presence brought new dangling bonds for GO, thus boosting its GO magnetic properties. Pristine GO nanosheets exhibited $r_1 = 0.210 \text{ (mg/ml}\cdot\text{s)}^{-1}$ versus the GO concentration on a 4.7 T MRI scanner. The Authors showed the ability to modulate GO magnetic properties by controlling the amounts of dangling bonds at the edge of nanoholes and analyzed the residual metals content by Inductively coupled plasma mass spectrometry (ICP-MS), reporting the presence of Fe (45 ppm), Mn (3.66 ppm), Ni (0.93 ppm) and Co (0.03 ppm). However, no quantification of the relaxivities contribution from those low concentration metallic impurities was performed. Mohanta and co-workers [35] observed that the GO relaxivities are influenced by the degree of oxidation (which is correlated to the quantity of oxygenated defects present on the graphene skeleton) and the Mn(II) concentration, which was quantified by EPR spectroscopy, corresponding to about 2910 ppm. Interestingly, they did not report any effect due to the presence of dangling bonds. The GO_80h sample showed $r_1 = 0.49 \text{ (mM}\cdot\text{s)}^{-1}$ (equivalent to $0.60 \text{ (mg/ml}\cdot\text{s)}^{-1}$) and $r_2 = 4.16 \text{ (mM}\cdot\text{s)}^{-1}$ ($6.19 \text{ (mg/ml}\cdot\text{s)}^{-1}$) at 9.4 T [35]. Peng and co-workers [36] studied a water dispersible 2D magnetic nanocomposite suitable as T_2 contrast agent based on hydrophobic manganese-doped ferrite nanoparticles loaded on GO by direct solvent evaporation. The measured r_1 and r_2 values of the pure hydrophilic GO sheets (as purchased from suppliers) at 7.0 T were 0.34 and $5.54 \text{ (mg/ml}\cdot\text{s)}^{-1}$, respectively [36]. The latter relaxivity values reported show a good agreement with Mohanta's values, considering negligible the effect of the different magnetic fields. However, we notice that the amount of Mn impurities differs by three order of magnitude (3.66 versus 2910 ppm) and the effect of the dangling bonds is not univocally reported except in Li's work.

Noticing the lack of knowledge about the relaxivities values of pristine GO, in the present study, we aimed to answer the question about the pristine GO relaxivities and the effects of GO structural defects and/or manganese impurities level. In order to verify the contribution of manganese on the relaxivity, we studied the intrinsic longitudinal and transverse relaxivities of highly purified GO nanosheets, synthesized using the modified Hummers method [37], by means of an extremely accurate contaminants cleaning protocol.

The highly purified GO samples were characterized with chemical and physical techniques (morphology, chemical composition, elemental analysis, spectroscopy, and imaging). Specifically, 1.0 T MRI measurements and X-band EPR were used to detect and quantify the effects on the r_1 and r_2 relaxivities of ppm levels of paramagnetic dangling bonds, as well as Mn impurities embedded in the GO samples. For comparison purposes, we also characterized standard manganese chloride water solutions to calibrate MRI quantification methods at 1.0 T and for reference purpose in EPR. Our experimental findings corroborate the conclusions that MRI relaxivity of pristine GO nanosheets arises from structural defects and, due to our extremely accurate

cleaning protocol, the residual ultra-low levels of manganese impurities embedded in the nanomaterial provide a negligible contribution.

Materials and methods

MnCl₂

The measured pH of the aqueous (Milli-Q, Millipore, Bedford, MA, USA) 0.044 mM Mn(II) ($\text{MnCl}_2\cdot 4\text{H}_2\text{O}$, Merck 5927, 99%) solution was 7.18 (pHmeter pH8+DHS BASIC, XS Instruments, Italy) at room temperature (RT).

Synthesis of GO

The Hummer's approach is the most used procedure to synthesize GO, although many variations are reported in the literature [28]. Here, we synthesized our GO sample by using a modified Hummers method [37], followed by a repeated cleaning procedure, as described in the following. GO was prepared from 5 g of graphite flakes (Sigma Aldrich 332461; 99%; size $>150 \mu\text{m}$). Oxidation was performed in 275 ml concentrated sulfuric acid (Aldrich 30743; 95%–97%) with 3.8 g sodium nitrate (Aldrich 221341; ACS reagent 99.0%) and 25 g potassium permanganate (Fluka 60459; 99%), at 0 °C (ice bath). After 5 d of reaction, 20 ml hydrogen peroxide (Aldrich 30743; 30%) was added to the suspension to eliminate the excess of permanganate. The solution (300 ml) was diluted to 2 l with 5% sulfuric acid and, after one day of sedimentation, 1 l of supernatant was removed and replaced with a mixture of water (1 l) and hydrogen peroxide (10 ml). After vigorous shaking lasting 10 min, the suspension was allowed to sediment overnight. The supernatant solution was removed and the solid was cleaned by means of repeated centrifugations (REMI NEYA8, India; 5800 rpm; 4800 g; 15 min). First, twelve centrifugations with an aqueous mixture of 5% (v/v) sulfuric acid and 0.3% (v/v) hydrogen peroxide, followed by three centrifugations with hydrochloric acid 4% (v/v; 3 times), and finally ten centrifugations with water until the pH reached neutrality. In each centrifugation step the volume of the falcon never exceeded 80% of the capacity of the test tube itself (i.e. 40 ml out of 50 ml total). At the end of the centrifugation steps, the solid was transferred to acetone (50 ml) and dried at 50 °C for 24 h, obtaining about 4.8 g of GO powder. Starting from the solid GO, aqueous solutions of different concentration were prepared for the measurements using ultrapure Milli-Q distilled water (Millipore, Bedford, MA, USA). The measured pH of 1 mg ml^{-1} GO in Milli-Q water was 6.03 at RT.

Raman spectroscopy (RS)

GO flakes dispersed in Milli-Q water were deposited, by drop-casting, from a dilute aqueous solution (0.3 mg ml^{-1} , volume of $15 \mu\text{l}$) of the material on a silicon substrate (SiO_2 , oxide thickness 270 nm). RS was performed using a LAB-RAM system (Horiba-Jobin Yvon- Japan, $\lambda = 633 \text{ nm}$, $1 \mu\text{m}$ spatial resolution, and about 2 cm^{-1} spectral resolution).

Inductively coupled plasma-mass spectrometry (ICP-MS)

Manganese contamination was determined by Thermofisher iCAP™ TQe ICP-MS instrument. For ICP-MS analysis, 8 mg of samples were mineralized with 2.65 ml of ultrapure aqua regia (nitric and hydrochloric acid, 1:3; Merck Life Science S.r.l., Italy) at 180 °C for 20 min by means of a microwave digester (Ethos One, Milestone, Bergamo, Italy) in closed polytetrafluoroethylene (PTFE) reactors. For aqua regia: Suprapur™ HCl 30% (Merck Life Science S.r.l., 1.00318); Suprapur™ HNO₃ 65% (Merck Life Science S.r.l., 1.00441). The microwave protocol consists of a heating ramp from 0 °C to 180 °C in 10 min, thermostat at 180° for 20 min and cooling down at RT. Mineralized samples were recovered with Milli-Q water and diluted to 100 ml, filtered through a 0.2 μm recycled cellulose syringe filter and subsequently diluted by a factor of 2. Measurements were performed in triplicate experiments. Mono and multi-element stock Trace-CERT® solutions for ICP calibration were purchased from Fluka Analytical, (Sigma-Aldrich, MO, USA) and Merck KGaA (Darmstadt, Germany). Matrix effect and instrumentation drift were monitored using a 20 μg l⁻¹ rhodium solution as Internal Standard for all the analyzed solutions. All the standard solutions were prepared in 1% of aqua regia.

Electron paramagnetic resonance (EPR)

Continuous-wave electron paramagnetic resonance (CW-EPR) spectra were obtained with a Bruker X-band (9.81 GHz) spectrometer (Bruker Biospin S.r.l., Milano, Italy) equipped with a Bruker 3122SHQE resonator. Spectrum acquisition parameters: central magnetic field of 350 mT; scan range 140 mT; 4096 data points; modulation frequency 100 kHz; modulation amplitude 1 mT; microwave power 10 mW.

All EPR measurements were done at RT, with undiluted GO nanosheets inserted in Suprasil EPR tubes of 3 mm internal diameter (ATS Life Sciences Wilmad, NJ, USA). The MnCl₂ sample was prepared as 1 mg ml⁻¹ aqueous solution, while about 3.3 mg of solid GO was directly inserted into the EPR tubes for measurements. EPR spectra were simulated by the Matlab toolbox Easyspin v. 6.0.0—dev.51 [38].

To evaluate the numbers of spin of paramagnetic centers in GO, we used two methods: the double integration of the simulated EPR spectrum and an approximated evaluation of the area below the experimental spectrum using the rule-of-thumb $A_{pp} \cdot \Delta B^2$, where ΔB is the line width and A_{pp} is the peak-to-peak height obtained from the experimental spectrum. Due to noise in the experimental spectra we observed some degree of variation in the Mn(II) line width values (4.7–6.4 mT). The different transition probability was considered [39, 40] to obtain the ratio between the two paramagnetic species.

Magnetic resonance imaging (MRI)

The MnCl₂ and GO samples suitable for MRI were prepared in aqueous solution (Milli-Q water), at different concentrations, in 2 ml PTFE/silicone septa glass vials (diameter 11.6 mm and height 31.4 mm), by sonicating up to 30 min

before measurements (with ultrasound bath LBS 2; frequency: 59 kHz; peak power: 450 W). MRI was performed with a 1.0 T preclinical M3 aspect imaging scanner (proton frequency of 45 MHz). The solenoid radiofrequency coil (3.5 cm inner diameter and 8 cm length) allowed the insertion of up to four vials at the same time.

The T_1 relaxation time was measured from axial spin echo images with: field of view (FOV) of 32 × 32 mm²; 1 mm in-plane resolution; 1 mm slice thickness; echo time (TE) = 4.1 ms and 18 different repetition time (TR) values (TR=100, 150, 200, 250, 300, 350, 400, 450, 500, 750, 1000, 1500, 2000, 2500, 3000, 3500, 4000, 5000 ms; two more values were used for the MnCl₂ samples: TR = 30, 50 ms). T_1 maps were calculated by the exponential signal recovery within each image voxel, and the T_1 value of each sample by the average of the corresponding vial's voxels. The unavailability of multi-echo spin echo sequences prevented the T_2 relaxation mapping from images. Thus, we used a fast spin echo sequence with echo train length equal to 128 and disabled gradients, allowing a whole-sample CPMG (Car-Purcell-Meiboom-Gill) acquisition of each single vial. In our experimental conditions, multiple echoes from a single vial (TE = 4.4 ms) were acquired, finally extracting T_2 from the echoes' amplitude exponential decay. Voxel intensities and CPMG echoes fits were performed by means of in-house developed Matlab scripts (The MathWorks, Inc., Natick, MA, USA) using a 3 parameters mono-exponential fitting based on the Levenberg–Marquardt nonlinear least-squares' algorithm. All MRI measurements were done at 22 ± 1 °C. Finally, the molar relaxivities r_1 and r_2 (mM·s)⁻¹ were calculated from the slope of the linear regression of 1/ T_1 (s⁻¹) and 1/ T_2 (s⁻¹) as a function of CA concentrations (mM).

Results

Raman spectroscopy

Figure 1 shows the Raman spectra of the solid GO sample, with the characteristic shape of graphene-based materials. The two peaks at 1336 and 1603 cm⁻¹ are assigned, respectively, to the D-band and G-band. The intensity ratio of the D and G bands (I_D/I_G) is currently used as an indirect estimation of the disorder within the GO material [41], and we found a value of 1.41.

Inductively coupled plasma-mass spectrometry (ICP-MS)

We found traces of Mn both in the starting commercial graphite (68 ppm) and in the synthesized GO (73 ppm), as measured by ICP-MS.

Electron paramagnetic resonance spectroscopy

The EPR spectrum of the MnCl₂ aqueous solution (figure 2(a)) shows the typical hyperfine structure consisting of six well-resolved lines [42]. The GO EPR measurements were performed directly on the solid sample (figures 2(b)–(d), black line), which showed a predominant narrow single line

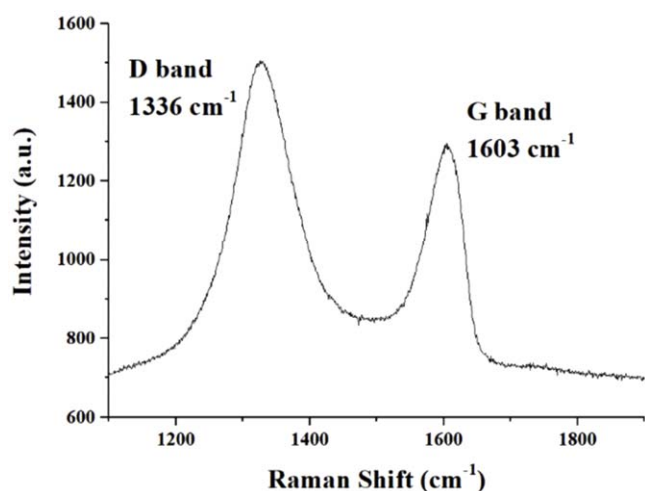


Figure 1. Raman spectrum of the GO sample synthesized in this work by the modified Hummers method [37].

centered around 350 mT. Enlarging the y-axis by a factor 80x, the pattern of six broad lines characteristic of isolated (i.e. non-interacting) Mn(II) ions is shown (figure 2(c), black line). The EPR line parameters were evaluated by the ‘pepper’ simulation function available in the Easyspin software [38], and they are shown in figures 2(a)–(d), as red lines. The spectra corresponding to the two contributions were simulated separately (figures 2(c) and (d), red line) and then used to give the overall spectrum (figure 2(b), red line). The narrow 350 mT line was simulated by a Lorentzian lineshape (0.22 mT line width, $g = 2.0031$). The six broad lines were simulated by a Lorentzian lineshape (6.4 mT line width, $g = 2.0031$). The EPR spectra provide evidence of both GO defects as well as small amount of Mn(II) embedded in the GO sample. The area under the EPR absorption spectrum of the two paramagnetic species was calculated by two different methods (see Materials and Methods section), to obtain a ratio between Mn(II) centers to paramagnetic defects in GO ranging from 4.3:1 to 1.7:1, due to the noise in the Mn(II) experimental spectrum.

Magnetic resonance imaging

We performed standard manganese chloride water solutions to calibrate MRI quantification methods. Figure 3 shows the 1.0 T acquired T_1 weighted-images (figure 3(a)) and CPMG echo amplitudes (figure 3(b)) of the MnCl_2 phantoms, with Mn(II) concentrations ranging from 0 to 1.0 mM. Relaxation rates $R_1 = 1/T_1$ and $R_2 = 1/T_2$ are plotted in figure 3(c). The linear regressions of the R_1 and R_2 data as a function of micromolar Mn(II) concentrations provide the relaxivities values and the coefficients of determination (R^2), as reported in figure 3(c). The measured molar relaxivities for the Mn(II) in water were, respectively, $r_1 = 5.7 \text{ (mM s)}^{-1}$ and $r_2 = 51.7 \text{ (mM s)}^{-1}$.

Figure 4 shows the T_1 -weighted images (figure 4(a)) and CPMG echo amplitudes (figure 4(b)) of GO in water. The linear regressions of the relaxation rate data as a function of the GO concentration in water are shown in figure 4(c). The relaxivities

values and coefficients of determination (R^2) are also reported. The measured molar relaxivities for the GO in water were, respectively, $r_1 = 0.21 \text{ (mg/ml s)}^{-1}$ and $r_2 = 1.44 \text{ (mg/ml s)}^{-1}$.

Discussion

GO is a nanoscale 2D inhomogeneous system presenting a patchwork of graphene-like regions (surviving from chemical exfoliation of graphite), oxygenated defects and nanoholes (typically covering 5% of GO) [43]. The GO defects can be classified into on-plane and in-plane [44], with the on-plane defects mainly due to epoxy/hydroxy groups located on the basal plane and carboxylic/carbonyl groups located on the border of GO sheets, while the in-plane are point defects, such as vacancies, substitutional or interstitial impurities (figure 5). One of the most controversial aspects regarding pristine GO concerns the origin of its paramagnetism. Currently, this is attributed to the presence of structural defects of the material itself [16, 24, 34], as well as to paramagnetic atoms embedded in the GO structure [18, 36]. To establish the effect and weight of both contributions, various characterization techniques were used to better understand the actual GO chemical structure and to quantify the presence of paramagnetic impurities.

Raman spectroscopy is a widely used method to characterize the structural features of carbon nanostructures, as this brings specific information on the presence and relative quantification of defects. The D-band peak (1336 cm^{-1} , D stands for disorder-induced) is a symmetry-breaking Raman signal, observed only in the presence of defects like vacancies, flake boundaries and edges. The D-band peak reveals structural imperfections induced by the presence of hydroxyl and epoxide groups on the carbon basal plane. The G-band peak is instead a characteristic of the graphene skeleton, and it is attributed to the first order E_{2g} phonon scattering of the sp^2 carbon-carbon bond [45]. The intensity ratio of the D and G bands (I_D/I_G) is currently used to estimate the number and size of the sp^2 domains within the GO material [41].

The D and G bands with similar intensities ($I_D/I_G \sim 1$) are typically observed in GO [46]. Usually no D-band peak is observed for graphite without defects or in the center of graphene layers, while it becomes predominant in the presence of sample edges, as in the case of GO [45].

The strong D band in the Raman spectrum (figure 1) confirms the successful introduction of oxygen groups (and defects) into our GO. In this sample, the I_D/I_G ratio is dramatically higher (1.41) than the one (0.05) previously reported for the commercial graphite material [45], suggesting the presence of a large number of functional groups and/or defects. The I_D/I_G ratio measured here is very similar to the ones ($I_D/I_G = 1.02$ – 2.5) reported by others [34, 35, 47].

The graphite commercial grade used for the GO synthesis already has structural defects, altering the final structure of GO and the presence of in-plane defects [48]. We used graphite with over 75% of the flake’s distribution having size of at least $150 \mu\text{m}$ (as per the manufacturer’s certificate of analysis). Large flakes of GO with smooth edges are found in the

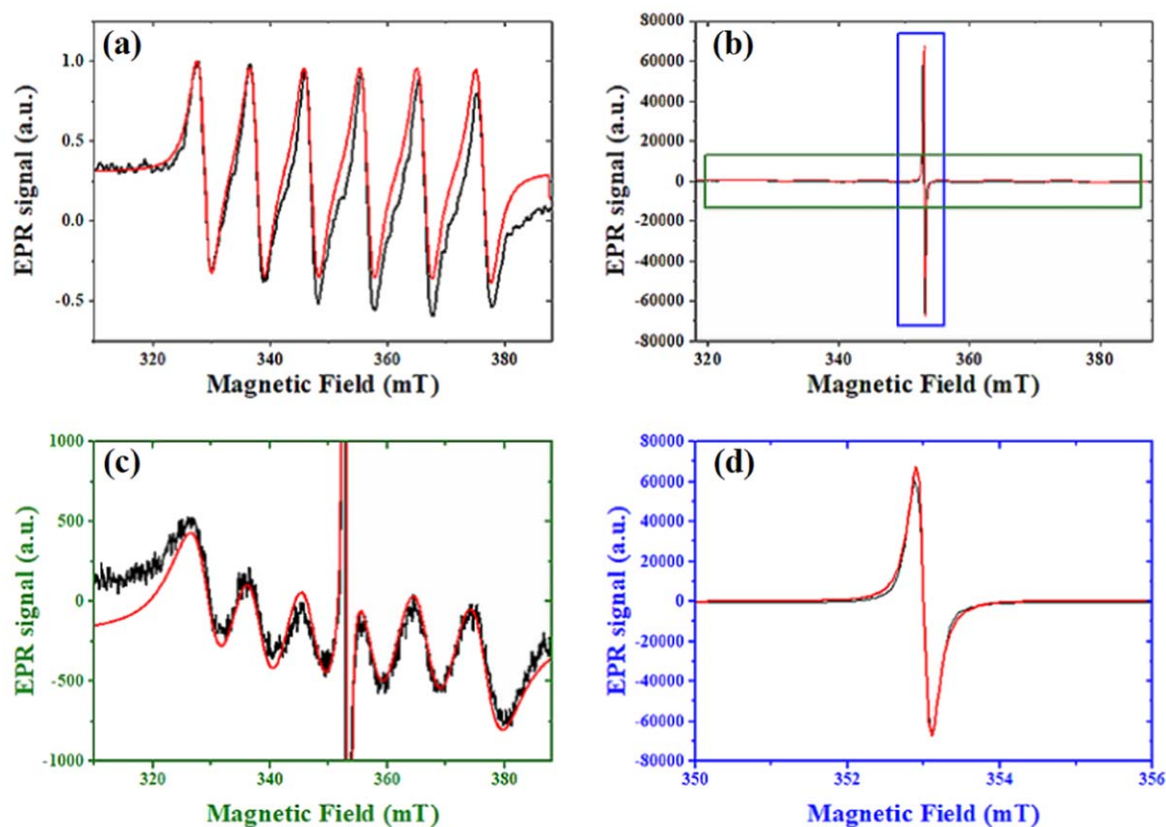


Figure 2. X-band EPR spectra of (a) MnCl_2 (1 mg ml^{-1}) aqueous solution, experimental spectrum (black) and simulated spectrum (red); (b)–(d) solid GO sample (3.3 mg) experimental spectrum (black) and simulated spectrum (red). The green and blue boxes highlight the Mn(II) and defect signals in GO, respectively. (c) Y-axis is enlarged by a factor 80x: experimental (black line) and simulated (red line) components. (d) X-axis is enlarged: experimental (black) and simulated (red) defect component.

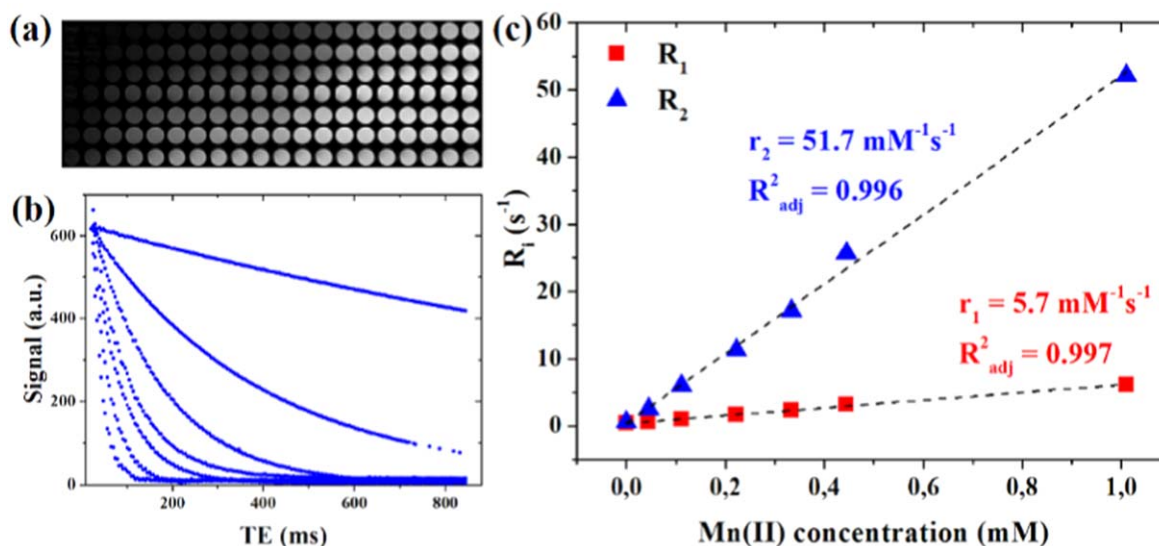


Figure 3. 1.0 T MRI of seven test tubes containing variable Mn(II) concentrations in water ($[\text{I}] = 0; 0.044; 0.111; 0.222; 0.333; 0.445; 1.011 \text{ mM}$). (a) T_1 -weighted images used for T_1 mapping (top to bottom: vials with increasing Mn concentration; left to right: TR values from 30 to 5000 ms); (b) CPMG echo amplitudes (188 echos, TE = 4.4 ms) for T_2 quantification of the seven test tubes; (c) relaxation rates $R_i = 1/T_i$ versus Mn(II) concentration (red squares for R_1 , blue triangles for R_2).

SEM images, with lateral flakes size of about $50\text{--}100 \mu\text{m}$ (figure S1), while the smallest GO flakes (down to $1\text{--}2 \mu\text{m}$) are the result of the sample sonication used to increase water dispersion. Sonication is likely to act mainly on the structural

vacancy points and holes, where the material is most prone to fragmentation.

The presence of structural defects in the GO can favor the insertion of paramagnetic contaminants into the structure

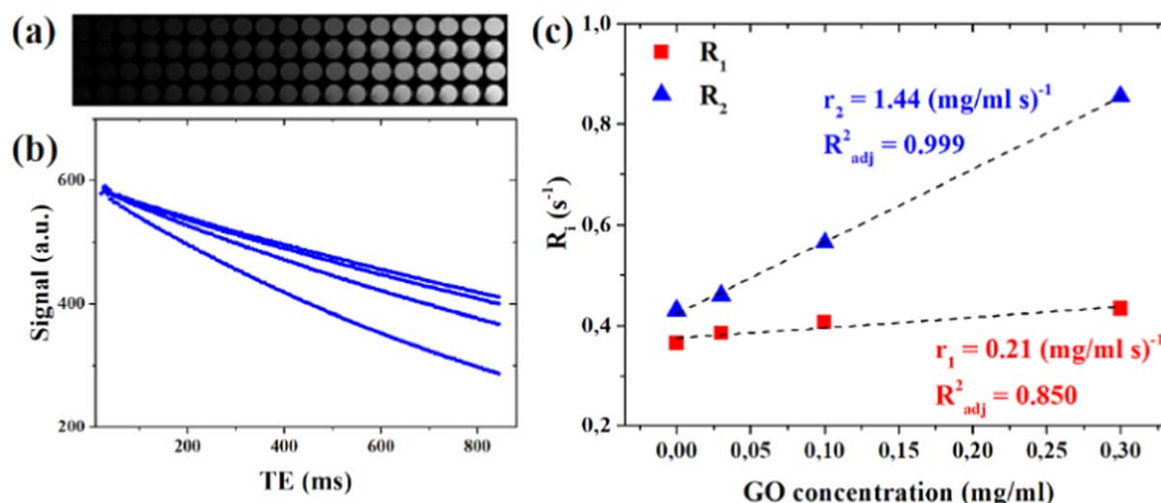


Figure 4. 1.0 T MRI of four test tubes containing variable GO concentrations in water ($[] = 0; 0.01; 0.1; 0.3$ mg ml $^{-1}$). (a) T_1 -weighted images used for T_1 mapping (top to bottom: vials with increasing GO concentration; left to right: TR values from 100 to 5000 ms); (b) CPMG echo amplitudes (188 echos; TE = 4.4 ms) for T_2 quantification of the four test tubes; (c) relaxation rates $R_i = 1/T_i$ versus GO concentration in water (red squares for R_1 , blue triangles for R_2).

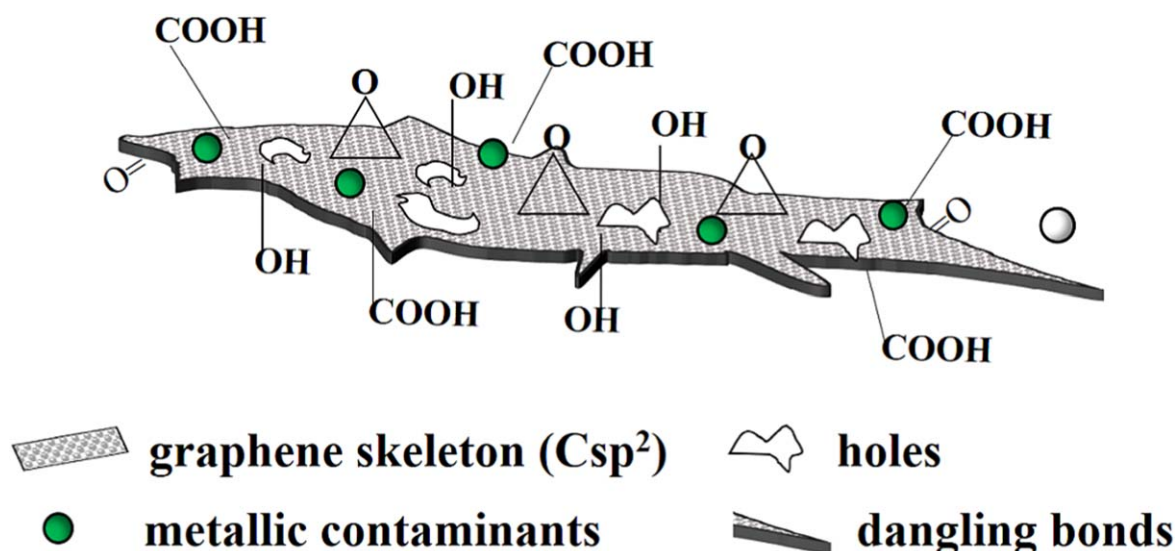


Figure 5. Schematic of a GO nanosheets including the Csp 2 skeleton, oxygenated defects, nanoholes, metallic contaminants, dangling bonds, epoxy/hydroxy groups located on the basal plane and carboxylic/carbonyl groups located on the border of GO sheet.

itself, acting as active MRI T_1 and/or T_2 contrast centers. From the literature, it appears that various oxygen functional groups and defects available on GO could bind to metal cations, via electrostatic interaction [49]. The interaction between ion metals and carboxylic acid groups on GO results in a slight shift of the carboxylic peak observed in XPS spectra at about 289 eV, overlapped with the pre-existing COOH peaks. It was also reported that epoxy bridge and carbon vacancies with a hydroxyl group are the most likely anchoring sites for metal particles, acting as nucleation sites [49].

The presence of the oxygen groups decorating the graphene skeleton in our sample was confirmed by Fourier transform infrared spectroscopy (see figure S3) and x-ray photoelectron spectroscopy (see figure S4), together with the occurrence of an aromatic graphenic structure. Within the

sensitivity limits of the XPS (1000 ppm), however, we found no trace of manganese in our GO sample (Mn 2p peak is expected around 640 eV, see figure S4(a)).

ICP-MS measurements of Mn(II) content in GO, as well as in other reagents, are shown in table 1 to compare our result (73 ppm) with the work of Wong *et al* [28], which previously reported an exceeding concentration of manganese of about 2290 ppm.

This difference can be attributed to our specific synthetic route, which employs repeated rinsing and centrifugation processes. Our procedure, although time consuming and relatively expensive, allows us to reduce to a minimum level the presence of Mn contaminants in our GO samples, considering that in the graphite oxidation process a stoichiometric excess of potassium permanganate was used. Moreover, in [28] the amount of Mn in the original high-grade purity

Table 1. Nominal (⁺) Mn concentrations within the reagents as stated by the manufacturers. The (*) symbol indicates ICP-MS measurements, the (***) symbol neutron activation analysis (NAA). Manganese values reported by Wong *et al* [28] are shown for comparison. We have used Milli-Q water instead of distilled water as in [28].

Sample	Mn (ppm) (this work)	Mn (ppm) [28]
H ₂ SO ₄	<1 ⁺	<0.01
NaNO ₃	<5 ⁺	<0.01
H ₂ O ₂	<2 ⁺	not reported
HCl	<0.01 ⁺	not used
Graphite	68*	0.14**
Graphene oxide	73*	2290**

graphite is about three orders of magnitude lower than in our graphite. In the comparison it must also be considered that Mn was measured with a different analytical method (neutron activation analysis).

In the literature, EPR spectra of GO always showed a single sharp and intense paramagnetic resonance peak with *g*-value of about 2.0031 [50]. The origin of spin species in pristine GO is likely to be related to some free radicals associated with broken bonds at structural defect sites [51]. It has been proposed that the free radicals could originate from graphite [23, 52] or be produced during the oxidation process due to the use of potassium permanganate or hydrogen peroxide [31]. The radical content in GO was intrinsically low, and, since OH radicals are highly unstable in aqueous solution or in air, it is assumed that the EPR signal of GO originates from single electron carbon radicals, which are temporarily stabilized by the π -conjugated double bonds [31]. A single EPR line suggests, in fact, an unpaired free electron, eventually bound to a nucleus with zero spin. Therefore, the EPR line originates from the carbon rather than from other radicals [53, 54]. It was shown that addition of H₂O₂ in the synthesis plays a role in removing the excess KMnO₄ and in reacting with GO by the addition of hydroxyl radicals to the double bonds of the disrupted π -network plane of GO, leading to the formation of a number of π -conjugated carbon radicals [31].

In the GO sample EPR spectrum (figures 2(b)–(d)), we confirmed the presence of a single intense and narrow line around 350 mT (*g* = 2.0031), that we ascribe to dangling bonds that do not complete the valence [34], as well as the presence of Mn(II) embedded in the GO structure (six hyperfine lines signal), while no lines typical of other paramagnetic metal impurities are detectable. The GO signal component may be associated with electrons localized at defect sites, as reported by Tampieri *et al* [55].

Li and co-authors [34] reported in the EPR spectrum an intense peak at 337–338 mT, due to GO defects and no evidence of the Mn signal. The amount of Mn measured in their samples by ICP-MS is significantly (about 20 times) less than what we measured, corresponding to about 4 ppm against our 73 ppm. This difference can be attributed to the fact that Li *et al*, before making ICP-MS measurements, centrifuged the GO aqueous sample at high rpm (12500 rpm) for 30 min, and

subsequently recovered only the supernatant. We argue that only very small-size monolayer GO sheets will preferably be present in the withdrawal (about 10 nm of lateral dimension, as reported in [34]).

On the contrary, in the EPR spectra of Mohanta [35] the Mn signal is much more evident than in our spectra (figure 2(b)), and much more intense than the central peak of the GO defects. In this case we may suppose that the sample cleaning procedure was probably not as effective as the one specifically developed by us, consisting in a multi-repetition cleaning procedure via ultra-centrifugation (5800 rpm; 4800 g; 15 min). The GO cleaning protocol adopted by Mohanta (as reported in the supporting information [44]) was simply based on washing the sample with DI water three times and twice with ethanol. The ICP-MS analysis confirmed in our samples much lower Mn quantities (at least a factor 40) with respect to Mohanta's work [35, 47].

From our EPR data, an absolute quantification of Mn(II) impurity in GO nanosheets was not attempted. In fact, quantitative EPR is very challenging, and many subtleties will affect the result [39]. For this reason, we adopted ICP-MS technique for Mn(II) quantification and used EPR spectra to estimate the relative concentration of Mn(II) and spin defects in GO. As reported in Materials and Methods section, the comparison of the relative abundance between two different paramagnetic species with different lineshapes is not straightforward in EPR, so we referred to [39, 40] and, taking into account the different transition probability, we calculated the ratio between the Mn and the defect centers, ranging from 4.3:1 to 1.7:1. The smaller fraction of structural defects compared to the manganese atoms gives them critical importance and effectiveness, being the former the main source of relaxation in MRI in our samples.

Moreover, we can confirm that this small amount of Mn(II) is bonded to GO nanosheets, since in our MRI measurements on the centrifuged supernatant GO water solution, we found no change in the *T*₁ and *T*₂ relaxation times with respect to the Milli-Q water, within the sensitivity limit of MRI.

The 1.0 T MRI acquired *T*₁ weighted-images and CPMG echo amplitudes of the aqueous manganese chloride solutions are reported in figure 3, with Mn(II) concentrations ranging from 0 to 1.0 m, and corresponding relaxation rates.

The measured molar relaxation rates are reported in table 2 together with previous data from literature [13, 56]. The relaxivities constant of Mn(II) ions in water obtained at 0.94 and 1.5 T [14] compare well with our results at 1.0 T, with minor differences probably due to the magnetic field intensities and/or temperature. The *r*₂/*r*₁ ratio, a sort of signature of the paramagnetic agent, is always close to 10.

In table 2 we also reported a different agent: MnDPDP, a Mn-based contrast agent with the paramagnetic atom chelated by DPDP agent to minimize toxicity. Teslascan relaxivities [14] were such that their ratio *r*₂/*r*₁ for MnDPDP is significantly lower than the ones of free Mn(II) ions, suggesting a reduced interplay of the water molecules with the surroundings of the paramagnetic agent as a consequence of the chelating molecule. We adopt the same approach to discuss

Table 2. The r_1 and r_2 values for Mn(II) ions in water at field comprised from about 0.94 to 1.5 T. The operating temperatures are also shown, when available. DPDP = DiPyridoxyl DiPhosphate.

Sample	Magnetic field (T)	T (°C)	r_1 (mM·s) ⁻¹	r_2 (mM·s) ⁻¹	References
Mn(II)	0.94	NA	6.0	57	[56]
Mn(II)	1.0	21.5	5.7	52	This work
Mn(II)	1.5	NA	7.0	70	[13]
MnDPDP (Teslascan)	1.5	37	1.6	2	[14]

Table 3. The r_1 and r_2 values for pristine GO in water at fields comprised from 1.0 to 9.4 T. The relaxivities of the GO samples are expressed as function of the GO concentration (mg/ml). The (*) and (**) symbols are referred to ICP-MS and EPR measurements, respectively. The operating temperature for our work was 22 °C, while no data are available from the references, unfortunately.

Sample	Magnetic field (T)	r_1 (mg/ml·s) ⁻¹	r_2 (mg/ml·s) ⁻¹	Mn (ppm)	References
GO	1.0	0.21	1.44	73*	This work
GO_80h ball milling	3.0	1.40	NA	2910**	[35, 47]
GO	4.7	0.21	NA	4*	[34]
GO	7.0	0.34	5.54	NA	[36]
GO_80h ball milling	9.4	0.60	6.19	2910**	[35, 47]

the GO relaxivity data with the expectation that both structural defects and embedded Mn impurities contribute to the r_1 and r_2 values.

In figure 4 we showed the T_1 -weighted images (figure 4(a)) and CPMG echo amplitudes (figure 4(b)) of GO in water, and the relaxation rate data as a function of the GO concentration in water (figure 4(c)). We noticed that at higher GO concentrations (>0.3 mg ml⁻¹) the aggregation of nanosheets occurred, providing relaxation rates deviations from the linear behavior. For this reason, higher concentrations were excluded from our analysis.

The measured molar relaxivities for the GO were reported in table 3, showing the r_1 and r_2 values of pristine GO (mg/ml) measured by us and the ones measured by other Authors [34–36]. Our relaxivities constants were, respectively, $r_1 = 0.21$ (mg/ml s)⁻¹ and $r_2 = 1.44$ (mg/ml s)⁻¹. The relaxivities measured between 1.0 and 9.4 T are of the same order of magnitude, while the measured Mn contamination ranges over three orders of magnitude. We also note that our r_2/r_1 ratio differs from 10, which is the ratio of the free Mn(II) ion, but is lower than Mohanta's work [35, 47] and still lower than Peng's work [36], suggesting different physical mechanisms of water relaxation at play.

It is reasonably to hypothesize that paramagnetic atoms contamination (more specifically Mn) may be the main origin of GO relaxivity in water. Under the above assumption we calculated the expected relaxivities, as a function of the equivalent molar Mn concentration in water (measured by ICP-MS). The values are reported in table 4, together with literature data that allowed the same transformation from GO to Mn molar concentration in water (using the published data of Mn content in the GO samples).

Our starting point is that relaxivity values at 1.0 T (table 4) of highly purified GO, versus ICP-MS measured Mn impurities concentration, are $r_1 = 155$ (mM·s)⁻¹ and $r_2 = 1076$ (mM·s)⁻¹ while Mn(II) free in solution values, at the same field, are $r_1 = 6$ (mM·s)⁻¹ and $r_2 = 52$ (mM·s)⁻¹.

Comparing relaxivities of GO and of Mn(II) free in solution we see that the former values are (i) much larger than the latter ones, and (ii) the r_2/r_1 ratio differs. This comparison suggests two main conclusions. First, the measured Mn impurities alone cannot explain the observed GO relaxivity because, even if Mn impurities were in free ionic form, they could be responsible only for a small fraction of the observed relaxivities. Such fraction is comprised between 1/30 and 1/20 which is the ratio of free ionic Mn(II) and GO relaxivities. Considering that our MRI measurements at 1.0 T gave no evidence of free ionic Mn(II) in GO samples, and that Mn linked to other structures generally has lower relaxivities (as for MnDPDP), we conclude that the actual contribution of Mn impurities to our GO samples relaxivities is even smaller than 1/30, i.e. negligible within our measurement accuracy. Second, the r_2/r_1 ratio in our GO samples is close to 7, not to 10 as for free ionic Mn(II), thus suggesting GO-water interactions differing from the ones of ionic Mn(II)-water. Both observations point towards the paramagnetic defects as the main source of pristine GO nanosheets relaxivities.

A quantitative comparison of relaxivities measured by other groups is not straightforward because of differences in magnetic fields, operating temperature (quite often not reported), flake sizes and dangling bond density. For example, lateral size dimension of our nanosheets is at least two orders of magnitude greater than others [16, 34–36, 47]. The presence of large GO's flakes can favor their re-aggregation in aqueous solution, a phenomenon to be avoided for biomedical applications. The sonication we performed on the aqueous GO, to improve its dispersibility, lasted 30 min, while making sure that the temperature did not rise significantly (always less than 40 °C). On the long term, we verified the GO stability in aqueous solution over few months after sonication, without observing the formation of sediments in the vials.

The Raman I_D/I_G ratio is similar between the different samples, considering that the synthetic procedure used is always the same (Hummers modified). Observing the values

Table 4. The r_1 and r_2 values for pristine GO normalized to the molar Mn concentration of GO impurities in water, at fields comprised from 0.47 to 9.4 T. The (*), (**) and (***) symbols indicate ICP-OES (Inductively-coupled plasma optical emission spectroscopy), ICP-MS and EPR measurements, respectively. The operating temperature for our work was 22 °C, while no data are available from the references.

Sample	Magnetic field (T)	r_1 (mM·s) ⁻¹	r_2 (mM·s) ⁻¹	References
GO in 1% Plu at 40 °C	0.47	52*	114*	[16]
GO	1.0	155**	1076**	This work
GO	4.7	3**	NA	[34]
GO_80h ball milling	9.4	0.5***	4***	[35, 47]

reported by Li *et al* [34] it can be seen that their data show the same r_1 of this work, but with a smaller amount of Mn impurities (4 ppm against 73 ppm). If we discard the difference in the measuring MRI field (4.7 versus 1.0 T), this is consistent with a negligible contribution of Mn to the total GO paramagnetism for the samples of both studies. Comparing the results of Mohanta *et al* [35, 47] at 3 T and this work we notice a much larger r_1 (7 times) associated with 40 times more Mn, which can be interpreted as a regime where the paramagnetic impurities may have become the dominant relaxation mechanism due to a poor cleansing method used. This is confirmed by the 9.4 T measurements from the same Authors, where the r_1 changes due to the different Larmor frequency, but the r_2/r_1 ratio is similar to the free ionic Mn(II). A comparison of our relaxivities with the one reported by Peng and co-authors [36] is not feasible, since they did not quantify the paramagnetic impurities (the sample was supplied by a commercial provider, and we expect the Mn concentration to be very large).

Even if we did not explore the results for GO sheet of different sizes, we expect our results to be relatively independent from this parameter. Indeed, the quantitative presence of defects due to contour edges (external as well as internal ones) has been demonstrated to be independent on the flake size [41].

Conclusions

In this work we confirmed that the GO structure is dense of oxygenated groups, carboxylic, epoxy and hydroxyl groups, as well as point defects, which give rise to a basal paramagnetism, and act as anchoring groups of residual Mn from the preparation reaction. Surely, there is still much to understand about the mechanism of action of GO as a contrast medium for MRI applications.

With this study we have contributed to understanding and disentangling the factors that influence the relaxivity properties of GO nanosheets in water dispersion, a new class of nanomaterials with a wide range of biomedical uses. From the wide literature review considered here and our experimental results, we conclude that, when a rigorous GO cleaning process is performed, the residual paramagnetic manganese impurities can be reduced such as to provide a negligible contribution to the relaxivities, and the main relaxation mechanism is due to the presence of defects in the GO structure. It is reasonable to predict that water relaxation

values, could be modulated depending on the GO flake size and dangling bonds density, but this open question is beyond the scope of this work. Moreover, we argue that Mn impurities of at least 1000 ppm level, when the r_2/r_1 ratio gets closer to the one of free ionic Mn(II), could give a measurable contribution in MRI applications.

By the experimental relaxivity results we should classify pristine GO as a negative contrast agent. Even if the relaxivity values, when expressed in mM·s⁻¹, are much larger compared to Gd chelated paramagnetic CAs, the direct use of pristine GO must still be proved. The GO sheets used in present work have a much larger molecular weight than Gd chelates, and the concentrations used for this work could not be attainable in living tissues.

GO defects are normally considered to be detrimental to the properties of the nanomaterials, but in specific cases, such as MRI, they can be a beneficial feature for the design of GO-based CAs. As recently reported in the literature [34, 35], the relaxivities can be further modulated by the capability to induce paramagnetic nanoholes at will, affecting contrast mechanisms.

In conclusion, the ability to rationally manipulate GO features opens new opportunities in designing theragnostic nanoparticles, through its unique advantage of surface tailoring with therapeutic agents (e.g. anticancer drugs and photosensitizers). Taking GO for example, the presence of carboxyl or epoxy groups on the material surface allows further functionalization by forming covalent or ionic bonds with other species. Moreover, the carboxy groups at the GO edges can react with amino or hydroxyl groups through acyl reactions, while the epoxy groups in the GO plane may provide active sites for ring opening reactions with amino groups. Covalent functionalization of GO greatly modulates its chemical–physical properties. It is increasingly accepted by the scientific community that defects are actually structural motifs that can be controlled and engineered to improve the properties of a large variety of materials, including GO-based MRI CAs [41].

Acknowledgments

We thank Dr Tiziana M Florio for her help in the early phase of this work. This work was supported by the CNR-SPIN Nano-Agents project. We also thank the University of L'Aquila for internal RIA funding. GDT thanks the University of L'Aquila (Department of Life, Health, and

Environmental Sciences) for a one-year research fellowship. This research was partially funded by the European Union—NextGenerationEU under the Italian Ministry of University and Research (MUR) National Innovation Ecosystem Grant ECS00000041—VITALITY (CUP E13C22001060006).

Data availability statement

All data that support the findings of this study are included within the article (and any supplementary files).

Author contributions

GF, AG, PF, LTDG, SC, GDT, FP, NDB, GP, LO and MA performed research; GF, AG, PF, SC, LO and MA contributed new reagents/analytic tools; GF, AG, PF, SC, GP, LO and MA analyzed data; GF, AG, GDT and MA wrote the paper. All the authors revised the final manuscript.

Competing interest statement

The authors declare no conflict of interest.

Classification

Physical Sciences; Applied Physical Sciences.

ORCID iDs

Giulia Fioravanti [ORCID iD](https://orcid.org/0000-0002-8653-9925) <https://orcid.org/0000-0002-8653-9925>

Angelo Galante [ORCID iD](https://orcid.org/0000-0002-3228-7785) <https://orcid.org/0000-0002-3228-7785>

Paola Fattibene [ORCID iD](https://orcid.org/0000-0002-8204-0414) <https://orcid.org/0000-0002-8204-0414>

Laura Torrieri Di Tullio [ORCID iD](https://orcid.org/0000-0002-6687-5788) <https://orcid.org/0000-0002-6687-5788>

Silvia Colacicchi [ORCID iD](https://orcid.org/0000-0001-5917-5663) <https://orcid.org/0000-0001-5917-5663>

Giorgio De Thomasis [ORCID iD](https://orcid.org/0000-0002-7613-7893) <https://orcid.org/0000-0002-7613-7893>

Gianni Profeta [ORCID iD](https://orcid.org/0000-0002-0535-7573) <https://orcid.org/0000-0002-0535-7573>

Luca Ottaviano [ORCID iD](https://orcid.org/0000-0001-5133-7541) <https://orcid.org/0000-0001-5133-7541>

Marcello Alecci [ORCID iD](https://orcid.org/0000-0002-3958-992X) <https://orcid.org/0000-0002-3958-992X>

References

- [1] Geim A K and Novoselov K S 2007 The rise of graphene *Nat. Mater.* **6** 183–91
- [2] Gu Z J, Zhu S, Yan L, Zhao F and Zhao Y L 2019 Graphene-based smart platforms for combined cancer therapy *Adv. Mater.* **31** 1800662
- [3] Nurunnabi M, Parvez K, Nafiujjaman M, Revuri V, Khan H A, Feng X and Lee Y-K 2015 Bioapplication of graphene oxide derivatives: drug/gene delivery, imaging, polymeric modification, toxicology, therapeutics and challenges *RSC Adv.* **5** 42141–61
- [4] Chung C, Kim Y-K, Shin D, Ryoo S-R, Hong B H and Min D-H 2013 Biomedical applications of graphene and graphene oxide *Acc. Chem. Res.* **46** 2211–24
- [5] Lin J, Chen X Y and Huang P 2016 Graphene-based nanomaterials for bioimaging *Adv. Drug Deliv. Rev.* **105** 242–54
- [6] Fan W, Yung B, Huang P and Chen X 2017 Nanotechnology for multimodal synergistic cancer therapy *Chem. Rev.* **117** 13566–638
- [7] Tofts P S 2003 *Quantitative MRI of the Brain: Measuring Changes Caused by Disease* (Wiley Online Books)
- [8] Lohrke J et al 2016 25 years of contrast-enhanced MRI: developments, current challenges and future perspectives *Adv. Ther.* **33** 1–28
- [9] Silva A C, Lee J H, Aoki L and Koretsky A R 2004 Manganese-enhanced magnetic resonance imaging (MEMRI): methodological and practical considerations *NMR Biomed.* **17** 532–43
- [10] Hao D, Ai T, Goerner F, Hu X, Runge V M and Tweedle M 2012 MRI contrast agents: basic chemistry and safety *J. Magn. Res. Imag.* **36** 1060–71
- [11] Jeon M, Halbert M V, Stephen Z R and Zhang M 2021 Iron oxide nanoparticles as T(1) contrast agents for magnetic resonance imaging: fundamentals, challenges, applications, and perspectives *Adv. Mater.* **33** e1906539
- [12] Lazzarini A, Colaiezzi R, Galante A, Passacantando M, Capista D, Ferella F, Alecci M and Crucianelli M 2022 Hybrid polyphenolic network/SPIONs aggregates with potential synergistic effects in MRI applications *Results Chem.* **4** 100387
- [13] Thangavel K and Saritas E U 2017 Aqueous paramagnetic solutions for MRI phantoms at 3 T: a detailed study on relaxivities *Turk. J. Electr. Eng. Comput.* **25** 2108–21
- [14] Rohrer M, Bauer H, Mintorovitch J, Requardt M and Weinmann H-J 2005 Comparison of magnetic properties of MRI contrast media solutions at different magnetic field strengths *Invest. Radiol.* **40** 715–24
- [15] Crossgrove J and Zheng W 2004 Manganese toxicity upon overexposure *NMR Biomed.* **17** 544–53
- [16] Paratala B S, Jacobson B D, Kanakia S, Francis L D and Sitharaman B 2012 Physicochemical characterization, and relaxometry studies of micro-graphite oxide, graphene nanoplatelets, and nanoribbons *PLoS One* **7** e38185
- [17] Kanakia S, Toussaint J D, Chowdhury S M, Lalwani G, Tembulkar T, Button T, Shroyer K R, Moore W and Sitharaman B 2013 Physicochemical characterization of a novel graphene-based magnetic resonance imaging contrast agent *Int. J. Nanomed.* **8** 2821–33
- [18] Peng E, Wang F H, Tan S H, Zheng B W, Li S F Y and Xue J M 2015 Tailoring a two-dimensional graphene oxide surface: dual T-1 and T-2 MRI contrast agent materials *J. Mater. Chem. B* **3** 5678–82
- [19] Zhang M X, Cao Y H, Chong Y, Ma Y F, Zhang H L, Deng Z W, Hu C H and Zhang Z J 2013 Graphene oxide based theranostic platform for T-1-weighted magnetic resonance imaging and drug delivery *ACS Appl. Mater. Inter.* **5** 13325–32
- [20] Moradi S, Akhavan O, Tayyebi A, Rahighi R, Mohammadzadeh M and Rad H R S 2015 Magnetite/dextran-functionalized graphene oxide nanosheets for *in vivo* positive contrast magnetic resonance imaging *RSC Adv.* **5** 47529–37
- [21] Zhang M, Liu X, Huang J, Wang L, Shen H, Luo Y, Li Z, Zhang H, Deng Z and Zhang Z 2018 Ultrasmall graphene oxide based T₁ MRI contrast agent for *in vitro* and *in vivo* labeling of human mesenchymal stem cells *Nanomed. Nanotechnol. Biol. Med.* **14** 2475–83
- [22] Shen J M, Huang G, Zhou X, Zou J, Yang Y, Chen Y F and Men S K 2014 Safety evaluation of graphene oxide-based magnetic nanocomposites as MRI contrast agents and drug delivery vehicles *RSC Adv.* **4** 50464–77

- [23] Nair R R, Sepioni M, Tsai I L, Lehtinen O, Keinonen J, Krashennikov A V, Thomson T, Geim A K and Grigorieva I V 2012 Spin-half paramagnetism in graphene induced by point defects *Nat. Phys.* **8** 199–202
- [24] Panich A M, Shames A I and Sergeev N A 2013 Paramagnetic impurities in graphene oxide *Appl. Magn. Reson.* **44** 107–16
- [25] De Thomas G, Galante A, Fioravanti G, Ottaviano L, Alecci M and Profeta G 2023 Spin–lattice relaxation time in water/graphene-oxide dispersion *J. Chem. Phys.* **158** 124709
- [26] Lalwani G, D'Agati M, Khan A M and Sitharaman B 2016 Toxicology of graphene-based nanomaterials *Adv. Drug. Deliv. Rev.* **105** 109–44
- [27] Ambrosi A, Chua C K, Khezri B, Sofer Z, Webster R D and Pumera M 2012 Chemically reduced graphene contains inherent metallic impurities present in parent natural and synthetic graphite *Proc. Natl. Acad. Sci. USA* **109** 12899–904
- [28] Wong C H A, Sofer Z, Kubesova M, Kucera J, Matejkova S and Pumera M 2014 Synthetic routes contaminate graphene materials with a whole spectrum of unanticipated metallic elements *Proc. Natl. Acad. Sci. USA* **111** 13774–9
- [29] Panich A M, Shames A I, Aleksenskii A E and Dideikin A 2012 Magnetic resonance evidence of manganese-graphene complexes in reduced graphene oxide *Solid State Commun.* **152** 466–8
- [30] Augustyniak-Jablokow M A, Tadzysak K, Strzelczyk R, Fedaruk R and Carmieli R 2019 Slow spin relaxation of paramagnetic centers in graphene oxide *Carbon* **152** 98–105
- [31] Yang L, Zhang R, Liu B, Wang J, Wang S, Han M-Y and Zhang Z 2014 π -conjugated carbon radicals at graphene oxide to initiate ultrastrong chemiluminescence *Angew. Chem. Int. Ed. Engl.* **53** 10109–13
- [32] Li J et al 2016 Adaption of the structure of carbon nanohybrids toward high-relaxivity for a new MRI contrast agent *RSC Adv.* **6** 58028–33
- [33] Chen Y et al 2014 Multifunctional graphene oxide-based triple stimuli-responsive nanotheranostics *Adv. Funct. Mater.* **24** 4386–96
- [34] Li J et al 2020 Preparing dangling bonds by nanoholes on graphene oxide nanosheets and their enhanced magnetism *RSC Adv.* **10** 36378–85
- [35] Mohanta Z, Gaonkar S K, Kumar M, Saini J, Tiwari V, Srivastava C and Atreya H S 2020 Influence of oxidation degree of graphene oxide on its nuclear relaxivity and contrast in MRI *ACS Omega* **5** 22131–9
- [36] Peng E, Wang F, Zheng B, Li S F Y and Xue J M 2015 Engineered water-soluble two-dimensional magnetic nanocomposites: towards highly magnetic relaxometric properties *Nanoscale* **7** 7819–32
- [37] Treossi E, Melucci M, Liscio A, Gazzano M, Samori P and Palermo V 2009 High-contrast visualization of graphene oxide on dye-sensitized glass, quartz, and silicon by fluorescence quenching *J. Am. Chem. Soc.* **131** 15576–7
- [38] Stoll S and Schweiger A 2006 EasySpin, a comprehensive software package for spectral simulation and analysis in EPR *J. Magn. Reson.* **178** 42–55
- [39] Eaton G R, Eaton S S, Barr D P and Weber R T 2010 *Quantitative EPR* (Springer)
- [40] Siebert D, Dahlem J and Nagy V 1994 Importance of transition-probability values for accurate EPR concentration measurements *Anal. Chem.* **66** 2640–6
- [41] Perrozzi F, Prezioso S and Ottaviano L 2015 Graphene oxide: from fundamentals to applications *J. Phys.-Condens. Mater.* **27** 013002
- [42] Abragam A and Bleaney B 2012 *Electron Paramagnetic Resonance of Transition Ions, Oxford Classic Texts in the Physical Sciences* (OUP Oxford University Press)
- [43] Gao W, Alemany L B, Ci L and Ajayan P M 2009 New insights into the structure and reduction of graphite oxide *Nat. Chem.* **1** 403–8
- [44] Feicht P and Eigler S 2018 Defects in graphene oxide as structural motifs *Chemnanomat* **4** 244–52
- [45] Ferrari A C et al 2006 Raman spectrum of graphene and graphene layers *Phys. Rev. Lett.* **97** 187401
- [46] Cancado L G, Jorio A, Ferreira E H M, Stavale F, Achete C A, Capaz R B, Moutinho M V O, Lombardo A, Kulmala T S and Ferrari A C 2011 Quantifying defects in graphene via Raman spectroscopy at different excitation energies *Nano Lett.* **11** 3190–6
- [47] Mohanta Z, Atreya H S and Srivastava C 2018 Correlation between defect density in mechanically milled graphite and total oxygen content of graphene oxide produced from oxidizing the milled graphite *Sci. Rep.* **8** 15773
- [48] Botas C, Alvarez P, Blanco C, Santamaria R, Granda M, Ares P, Rodriguez-Reinoso F and Menendez R 2012 The effect of the parent graphite on the structure of graphene oxide *Carbon* **50** 275–82
- [49] Han D J, Kim S and Cho E S 2021 Revealing the role of defects in graphene oxide in the evolution of magnesium nanocrystals and the resulting effects on hydrogen storage *J. Mater. Chem. A* **9** 9875–81
- [50] Hou X-L, Li J-L, Drew S C, Tang B, Sun L and Wang X-G 2013 Tuning radical species in graphene oxide in aqueous solution by photoirradiation *J. Phys. Chem. C* **117** 6788–93
- [51] Komeily-Nia Z, Chen J, Nasri-Nasrabadi B, Lei W, Yuan B, Zhang J, Qu L, Gupta A and Li J 2020 The key structural features governing the free radicals and catalytic activity of graphite/graphene oxide *Phys. Chem. Chem. Phys.* **22** 3112–21
- [52] Chen L L, Guo L W, Li Z L, Zhang H, Lin J J, Huang J, Jin S F and Chen X L 2013 Towards intrinsic magnetism of graphene sheets with irregular zigzag edges *Sci. Rep.* **3** 2599
- [53] Kempirski M, Łoś S, Florczak P, Kempirski W and Jurga S 2017 EPR and impedance measurements of graphene oxide and reduced graphene oxide *Acta Phys. Pol. A* **132** 81–5
- [54] Wang B, Fielding A J and Dryfe R A W 2019 Electron paramagnetic resonance as a structural tool to study graphene oxide: potential dependence of the EPR response *J. Phys. Chem. C* **123** 22556–63
- [55] Tampieri F, Silvestrini S, Riccò R, Maggini M and Barbon A 2014 A comparative electron paramagnetic resonance study of expanded graphites and graphene *J. Mater. Chem. C* **2** 8105–12
- [56] Kreft B P, Baba Y, Tanimoto A, Finn J P and Stark D D 1993 Orally administered manganese chloride: enhanced detection of hepatic tumors in rats *Radiology* **186** 543–8